Chemical Dynamics Simulations of High Energy Xenon Atom Collisions with the {0001} Surface of Hexagonal Ice
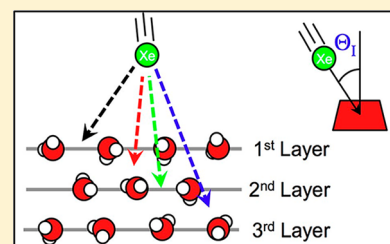
S. Pratihar,[‡] S. C. Kohale,[‡] L. Yang,[‡] P. Manikandan,[‡] K. D. Gibson,[§] D. R. Killelea,[§,†] H. Yuan,[§] S. J. Sibener,[§] and W. L. Hase[‡,*]

[‡]Department of Chemistry and Biochemistry, Texas Tech University, Lubbock, Texas 79409, United States
[§]The James Frank Institute and Department of Chemistry, University of Chicago, 929 East 57th Street Chicago, Illinois 60637, United States

ABSTRACT: Simulation results are presented for Xe atoms colliding with the {0001} surface of hexagonal ice (I_h) with incident energies E_I of 3.88, 4.56, 5.71, and 6.50 eV and incident angles θ_I of 0, 25, 45, and 65°. The TIP4P model was used for ice and ab initio calculations were performed to determine an accurate Xe/ice potential. Three types of events were observed; that is penetration below the ice surface and then desorption, penetration with Xe remaining in ice for times greater than 6 ps trajectory, and direct scattering without surface penetration. Surface penetration is most probable for normal ($\theta_I = 0°$) collisions and direct scattering becomes important for $\theta_I = 45°$ and 65°. Penetration into ice becomes deeper as E_I is increased. For $\theta_I = 0$ and 25°, all of the Xe atoms penetrate the surface and there is no direct scattering. The probability that the Xe atoms remain trapped below the surface increases as E_I is increased and is more than 70% for $\theta_I = 0°$ and $E_I = 6.50$ eV. For θ_I of 0 and 25° the trapped Xe atoms have a thermal energy of ~25 meV at 6 ps and are close to being thermalized. For θ_I of 0 and 25° the average translational energy of the scattered Xe-atoms $\langle E_F \rangle$ is highest when θ_F is very close to normal and then gradually decreases for higher values of θ_F. For θ_I of 45 and 65°, $\langle E_F \rangle$ is less than 250 meV for θ_F varying from 0 to 40°, but for larger θ_F the value of $\langle E_F \rangle$ rapidly increases to ~$1/3$ to $1/2$ of the collision energy. The probability of the subsurface Xe desorbing is greatest between 0 and 3 ps, with as much as 65% of the desorption occurring within a 1 ps interval of this time frame. Desorption is greatly diminished at longer times consistent with Xe becoming more thermalized. Simulation results using the TIP3P model for ice are similar to those above for the TIP4P model, with the caveat that trapping below the ice surface is more pronounced for the TIP3P model. The simulation results are in overall quite good agreement with experiment.

I. INTRODUCTION

Trapping of gas molecules is an important step in surface chemistry and many surface reactions are initiated with the adsorption of gas phase projectiles. The yield of surface catalyzed products is often small if the trapping probability is small. Efficient dissipation of the collision energy is important for a colliding atom or molecule to become trapped in a surface potential energy well. For example, the catalytic role of polar stratospheric clouds (PSCs)[1] in ozone layer depletion requires trapping of gas molecules, which may diffuse on the ice surface and react with other adsorbed or gaseous species to form products.

The interactions of molecules with an ice surface are of special interest in atmospheric chemistry[2] and chemical evolution in space.[3] A number of gas/ice surface interaction studies were reported using various methods.[4−8] Glebov et al.[9] and Braun et al.[10] investigated scattering of He atoms from crystalline ice surfaces grown at 125 K. Molecular beam experiments of N_2 scattering from ice surface for low incident energy have been performed by Gotthold and Sitz.[11] At normal incidence an energy loss of 85% for inelastically scattered N_2 molecules was observed. The trapping probability of N_2 on the ice surface was found to be 0.77 for an incident energy of 0.75 eV. Sticking probabilities for H_2O,[12] HCl,[13] HBr,[14] and NH_3[15]

on ice surfaces have been studied by molecular beam scattering experiments. Recently, Gibson et al.[16] investigated scattering of D_2O from an ice surface at a low incident translational energy of 0.3 eV. A barrier for penetration of NH_3 into the ice surface was estimated to be ~0.28 eV.[15] Experiments have suggested that Xe penetrates ice and forms clathrate cages.[17] Later experiments indicated there may be an induction period to form the clathrates.[18] More recent experiments by Gibson et al.[19] show that both Xe and Kr can penetrate ice and become trapped.

The dynamics of Ar collisions with ice had been studied by Anderson et al.[20] using both molecular beam experiments and theoretical simulations. It was observed that the Ar-ice surface collisions were highly inelastic, and thermal desorption dominated for incident kinetic energies of Ar below 1 eV. The energy loss to the surface was high reaching values up to 90% depending on the collision conditions and was largest at perpendicular collisions with the surface. Simulations of $O(^3P)$[21] and Ar[22] colliding with ordered self-assembled monolayer (SAM) surfaces grown on an Au(s) substrate have
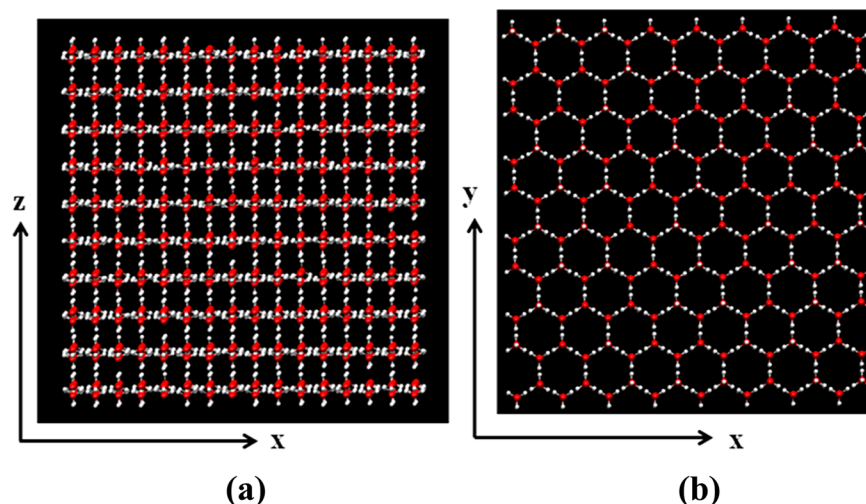
(a) **(b)**

Figure 1. Prefect crystal structure of hexagonal ice (I_h): (a) view in x–z plane, (b) basal x–y plane {0001}. The red and white spheres represent oxygen and hydrogen atoms, respectively.

been reported. Like ice, the SAM surface can absorb much of the incident energy of the colliding atom. Atoms can also penetrate well below the SAM surface, though this mechanism may be enhanced by the continuous channels between neighboring alkane chains all of the way to the Au substrate.

Recently, molecular beam experiments of Xe and Kr colliding with crystalline ice and amorphous solid water had been performed by Gibson et at.[23] This study was performed for Xe and Kr atoms with average incident energies ($\langle E_I \rangle$) between 1 and 6.5 eV and as a function of incident angle (θ_I) and scattering angle (θ_F). Two distinct velocity distributions in the post-collision time-of-flight spectra were observed, and both were attributed to interactions with the ice surface. The slower component, apparently due to thermal desorption, had a Maxwell–Boltzmann distribution with an average final energy, $\langle E_F \rangle$, of $2k_B T_S$, where k_B is Boltzmann's constant and T_S is the surface temperature. Such incident atoms got transiently trapped and thermally equilibrated with the surface before desorbing and, thus, lost all memory of the initial energy and angle. The faster component appeared to result from direct inelastically scattered (IS) atoms, where $\langle E_F \rangle$ showed direct dependence on θ_I, $\langle E_I \rangle$, and θ_F. A preliminary and incomplete simulation study, to assist in interpreting the experiments, was included with this work.[23] Both the experiments and the simulations indicated that penetration into the ice surface by the rare gas atoms is important.

Computational studies of HF[24] and HCl[25] colliding with the {0001} face of ice I_h has been done. One particular feature was that with sufficient E_I and, at $\theta_I \sim 0°$, these molecules penetrated well below the ice surface. For the HF molecule, it was reported that penetration into ice even occurred at very low incidence energies, viz., $E_I \sim 0.2$ eV, whereas penetration of HCl occurred at a higher E_I of approximately 1 eV. The penetration was attributed to the open structure of the ice crystal. At more grazing θ_I, the incident molecules no longer penetrated, and the interaction occurred only at the ice surface.

In the present article, a detailed chemical dynamics simulations study is reported for Xe atom collisions with the {0001} surface of hexagonal ice (I_h) providing complete results for the earlier preliminary and partial study.[23] As a function of the incident energy and angle, the article presents: the probability of Xe atoms penetrating the ice surface, and the

probability they remain trapped below the surface; the depth of penetration of the Xe atoms; and the energy and angular distributions for the Xe atoms that directly scatter off the surface and those that penetrate below the surface and subsequently desorb. A detailed comparison between the simulations and experiments[23] is also presented.

The paper is organized as follows. In section II, details of potential energy surfaces used to describe ice, Xe-water intermolecular interactions, and the method used to generate trajectories, are described. The results are presented and discussed in section III. The article ends with a conclusion in section IV.

II. SIMULATION MODELS AND COMPUTATIONAL METHODOLOGY

A. Model for Ice. The majority of the simulations reported here were performed employing the TIP4P[26] model for the water molecules, with a small number performed using the TIP3P[26] model to assess the sensitivity of the results on the model. Both are two-body potential energy functions. TIP3P is a three site model, with the charges of the H (+0.417) and O (−0.834) atoms explicitly represented. TIP4P is a four site model, which puts the negative charge (−1.04) on a dummy atom placed near the oxygen along the bisector of the HOH angle and positive charges (+0.52) on each hydrogen atom. This improves the electrostatic distribution of the water molecule. TIP4P has been used successfully in simulations of a variety of water systems including bulk liquid water,[26] the ice–water interface,[27] bulk crystalline,[28] and amorphous ice.[29] This model has also been used in studies of the structure and dynamics of ice I_h surfaces at temperature between 90 and 250 K[30] and trapping and sticking probabilities of HCl[31] and HOCl[32] on ice surfaces. Both TIP3P and TIP4P models assume rigid water molecules, and for the work reported here it is important to include the possibility of collision energy transfer to the intramolecular vibrational modes of the water molecules. This is expected to more accurately represent collision energy transfer to the ice surface and possible absorption of the Xe atoms. Accordingly, a harmonic intramolecular potential is included for each water molecule, with a stretching force constant[33] of 8.4 mdyn/Å and a bending force constant of 0.70 mdyn-Å/rad.[2] In future work, it will be of

interest to consider the effect(s) of rigid water molecules on the dynamics of projectile−ice collisions.

The hyperthermal Xe/ice simulation study reported here is for hexagonal ice (I_h). The specific model of hexagonal ice (I_h) used for the simulations consists of 10 bilayers with 1600 water molecules, which has been constructed from the unit cell reported by Hayward and Reimer.[34] The perfect crystalline structure of this model is illustrated in Figure 1. Part b of Figure 1 depicts the model's basal (x−y) plane. This ice model is similar to those used previously.[35] To study scattering of alkali ions from an ice surface Lahaye[35] used a large ice model, similar to the one used here. Periodic boundary conditions (PBC) were not included because of complications that would arise from possible damage to the ice surface by the hyperthermal Xe atom collisions. Such defects should not be incorporated into the PBC.[35]

Geometrical optimization of this ice model at 0 K, including the intramolecular degrees of freedom, yields a stable hexagonal ice structure. This structure is also stable at 140 K, the temperature of the simulations. The 140 K structure is depicted in Figure 2, which includes line density distributions of the O-atoms in the bilayers and a snapshot of the equilibrated structure.
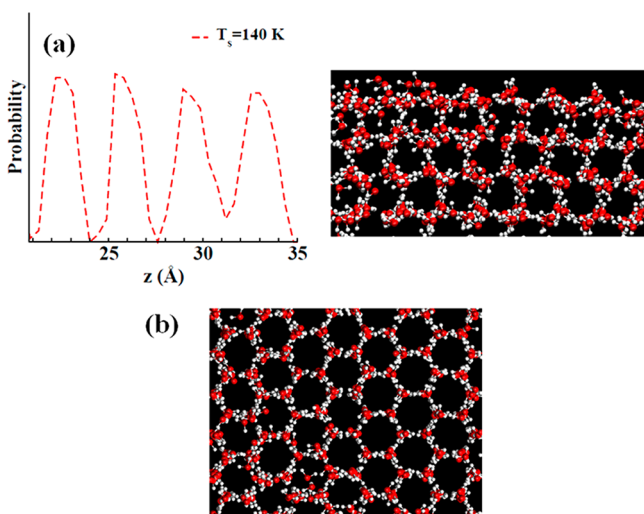

Figure 2. (a) Line density distribution at 140 K of the O-atoms in the top four bilayers of the hexagonal ice (I_h) model used for the simulations. Right panel shows a snapshot of the top four bilayers (x−z plane) of the 140 K equilibrated ice model. (b) Snapshot of the {0001} plane of 140 K equilibrated ice model. Red and white spheres have the same meaning as in Figure 1.

B. Xe−Ice Interaction. Ab initio electronic structure calculations and fits were used to develop an analytic intermolecular potential for Xe interacting with the ice surface. The MP2/aug-cc-pVDZ (LANL2DZ[36] for Xe) level of theory, with basis set superposition error (BSSE) corrections,[37] was used to calculate intermolecular potential curves for Xe interacting with H_2O and $(H_2O)_2$. For each of these systems two orientations, focusing on the Xe−O and Xe−H interactions, were considered in calculating the curves shown in Figure 3. The intermolecular potential energy curve for each of these orientations emphasizes a particular atom−atom interaction. The two curves for Xe/H_2O were fit simultaneously by a sum of two-body interactions between Xe and the O and H atoms, given by
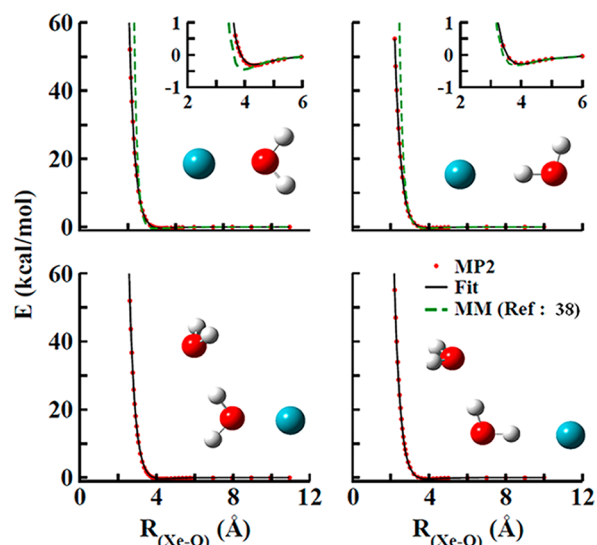

Figure 3. Intermolecular potential curves for Xe interacting with H_2O and $(H_2O)_2$. Top panel: Fitted analytic potential energy function is compared to the ab initio points for Xe interacting with the H_2O monomer in two different orientations. MM data from ref 38. have been plotted. The inserts provide a better resolution to illustrate comparison between the present fit and MM potential function from ref 38. Bottom panel: Ab inito and present fit data have been plotted for Xe interacting with $(H_2O)_2$. The scaling of the axes is same for all four plots. Xenon is represented by a green sphere. Red and white spheres have the same meaning as Figure 1.

$$V_{xy} = A_{xy}\exp(-B_{xy}r) + \frac{C_{xy}}{r^n} + \frac{D_{xy}}{r^m}$$

(1)

where the D_{xy}/r^m term is added to the Buckingham potential to provide additional flexibility in the fitting. The resulting fits are shown in Figure 3, and the fitted parameters are listed in Table 1. This fitted analytic intermolecular potential also gives an

Table 1. Parameters for the Xe−H and Xe−O Two Body Interactions[a]

	Xe−H	Xe−O
A (kcal/mol)	13 611.7	90 903.5
B (kcal/mol)	3.25177	3.14436
C (kcal/mol)	−1743.24	−8774.70
D (kcal/mol)	2430.85	0.0001397876
n	7	7
m	9	9

[a]The parameters were determined by fitting ab initio calculations, see text.

excellent fit to the two Xe/$(H_2O)_2$ potential energy curves also shown in Figure 3. Apparently, the presence of another water molecule has only a negligible effect on the Xe/H_2O interaction.

In a previous study a molecular mechanical (MM) intermolecular potential was developed for the Xe/H_2O two-body interactions.[38] As shown in Figure 3, for the two Xe/H_2O orientations considered here, the potential energy curves of the MM model are in approximate agreement with the ab initio curves calculated here. The current two-body potentials give potential minima of: −0.223 kcal/mol, 4.050 Å for Xe−O and −0.086 kcal/mol, 3.585 Å for Xe−H. The MM function gives

minima of: −0.270 kcal/mol, 3.871 Å for Xe−O; and −0.151 kcal/mol, 3.071 Å for Xe−H.

C. Trajectory Simulation Procedure. Classical chemical dynamics simulations of Xe atoms colliding with the basal {0001} plane of a hexagonal ice slab were performed using the general chemical dynamics computer program VENUS.[39,40] Initial conditions for the trajectories were chosen to model experiments by Sibener and co-workers.[23] The initial translational energy E_I of the xenon atoms was varied from 3.88 to 6.5 eV. The incident angle (θ_I), defined by the angle between the initial velocity vector of the Xe atoms and the surface normal, was varied from 0 to 65° (part a of Figure 4). To simulate the
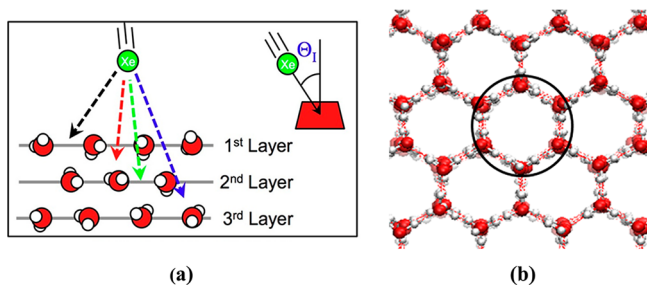

Figure 4. (a) Cartoon describing the incident angle (θ_I), and various penetration depths in terms of layers of water molecules along the normal of the {0001} plane of the ice surface. (b) Surface area of a unit cell on the {0001} plane of the ice surface. Red and white spheres have the same meaning as Figure 1.

Xe + ice collisions, a randomly sampled circular beam of xenon atoms[41,42] was directed toward the ice surface so that the area spanned by the beam covered a unit water hexamer (part b of Figure 4) on the ice surface. The center of the beam of Xe atoms was placed 8 Å above the 140 K thermalized ice surface. A molecular dynamics simulation[43] was performed to choose random initial coordinates and momenta for the 140 K ice surface.

To maintain the bulk ice crystalline structure for the ice model, initial test simulations were done with the atomic coordinates of the water molecules in the bottom two bilayers fixed at their 0 K optimized positions. The water molecules in the upper eight bilayers were thermalized at $T_s = 140$ K before initiating the Xe atom collision with the {0001} plane of the ice. It was found that the Xe atoms only penetrated as deep as the third bilayer (part a of Figure 4) and tests showed that the results remain the same by using models with fewer thermalized bilayers. Thus, to reduce the computer time required for the simulations, only the top six bilayers have been thermalized and allowed to move in the simulations, whereas the bottom four bilayers were held fixed at their 0 K optimized positions.

An Adams-Moulton algorithm, a standard option in VENUS, was used to integrate the trajectories. An integration time step of 0.2 fs was used, which conserved energy to seven significant figures. A total of 400 trajectories were calculated for each collisional energy and incident angle combination. Each trajectory was numerically integrated for 6 ps. The trajectories were analyzed for the translational energy distribution of both trapped and scattered Xe atoms. Also, distributions of the final scattering angle (θ_F), defined by the angle between the final velocity vector of Xe and the surface normal, were computed. The scattered Xe atoms were collected at all azimuthal angles and, thus, the θ_F distribution is proportional to $\sin\theta\cos\theta$ for isotropic scattering. The trapping lifetimes were analyzed for

the trajectories that penetrate the surface and then desorb. For the highest collision energy considered here of 6.5 eV, a Xe atom trapped below the surface increases the temperature of the ice model ∼18 K once the atom is thermalized.

III. SIMULATION RESULTS AND DISCUSSION

Xe collision energies E_I of 3.88, 4.56, 5.71, and 6.50 eV were considered and for each the angle of incidence, θ_I, was varied from 0 to 65°. The scattered Xe atoms were collected as a function of θ_F and over all values of the azimuthal angle from 0 to 2π. The Xe atoms either directly scattered off or penetrated the ice surface. For the latter, the Xe atom either desorbed from the ice or remained trapped below the surface during the 6 ps integration time of the trajectory. A representative trajectory which penetrates the ice surface and desorbs is depicted in Figure 5. The following results are for the TIP4P model for ice. Results for the TIP3P model of ice are given for comparison at the end of this section.
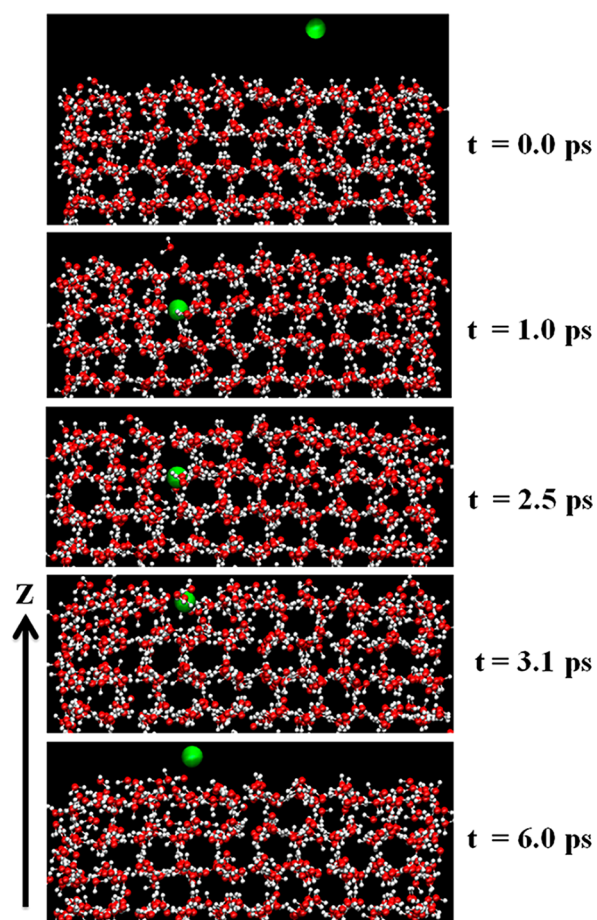

Figure 5. Time evolution of a trajectory, where Xe has undergone trapping-desorption. The snapshots were taken at different times during the 6 ps trajectory. The green, red, and white spheres represent xenon, oxygen, and hydrogen atoms, respectively. Times for the snapshots are reported on the right.

A. Surface Penetration. The probability the Xe projectile penetrates the ice surface for the different E_I,θ_I combinations is plotted in Figure 6 versus the depth of penetration. (The depth of penetration is defined along the z axis, part a of Figure 1, and structure along this axis, part a of Figure 4.) For a penetrating trajectory, the simulations show that when a Xe atom hits the
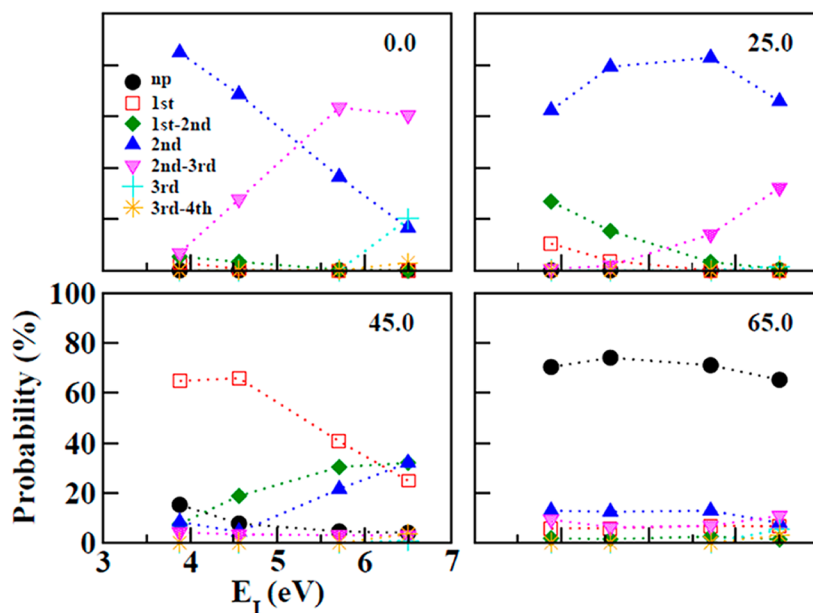
Figure 6. Probabilities of the deepest penetration depth of the Xe atoms inside the ice surface for different E_I and θ_I. Number at the top corner of each plot gives θ_I. The scaling of the axes is same for all four plots. The symbols identify the deepest penetration of the Xe atoms.

top of the unit water hexamer, the six water molecules undergo a concerted motion in the $x-y$ plane, and the hexagon enlarges and opens up a channel for the Xe to penetrate inside the ice surface. Similar observations were reported by Bolton et al.[44] for Ar-ice collisions. The penetration is deepest for $\theta_I = 0°$, as deep as between the third and fourth bilayers. For more grazing angles of incidence penetration becomes less probable and for $\theta_I = 65°$ no penetration becomes the most probable event. The Xe atoms penetrate deeper as the collision energy is increased and the results for $\theta_I = 0°$ are instructive. Xe atoms with $E_I = 3.88$, 4.56, and 5.71 eV can penetrate to the second bilayer, whereas with $E_I = 6.50$ eV penetration is to the third bilayer. It is of interest that there is a linear decrease in the probability of penetration to only the second bilayer as the collision energy is increased, and in future work it would be of interest to investigate whether this is related to the mechanism of penetration and/or the Xe + ice energy transfer dynamics. For θ_I of 0 and 25° all of the Xe projectiles penetrate the ice surface. For θ_I of 45 and 65° this is not the case, and direct scattering without penetration becomes important.

B. Trapping of Xe Atoms. For each E_I,θ_I combination, the probability was calculated that the Xe atoms remain trapped below the surface at the end of the trajectory integration at 6 ps. As shown in Figure 7, this trapping probability has a direct dependence on both E_I and θ_I. For all E_I's the trapping probability is largest for the 0° angle of incidence. With an increase in the incident angle, the probability the Xe atoms remain trapped decreases monotonically as a function of θ_I. For a particular incident angle θ_I, the trapping probability is greatest for the largest E_I. Thus, penetration and trapping in the ice surface is enhanced by collisions with normal incidence and high translational energy, and for $E_I = 6.50$ eV and $\theta_I = 0°$ it is higher than 60%! Of interest is the percentage of the trajectories which penetrate the ice surface, but then desorb during the 6 ps trajectory integration. For the $\theta_I = 0°$ simulations, this percentage is 70, 52, 39, and 27% for E_I of 3.88, 4.56, 5.71, and 6.50 eV, respectively. For $\theta_I = 25°$ these respective percentages are 82, 79, 56, and 43%; for $\theta_I = 45°$
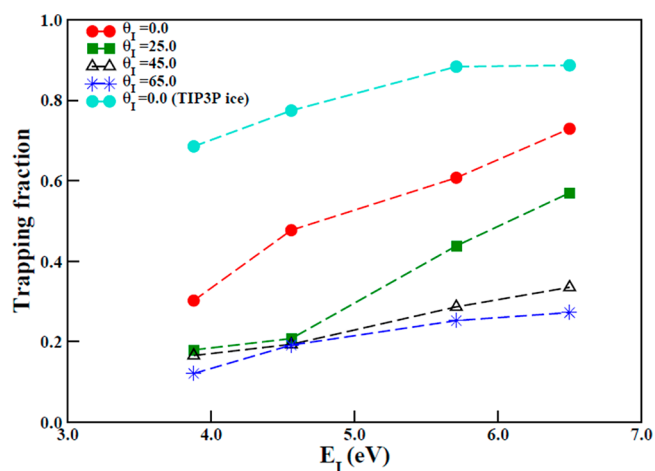

Figure 7. Probability (based on the total number of trajectories) the Xe atoms remain trapped inside the ice surface at the end of 6 ps simulation trajectories. Results are given for different E_I,θ_I combinations.

they are 80, 79, 70, and 65%; and for $\theta_I = 65°$ they are 59, 26, 13, and 22%. Less desorption with higher collision energy is consistent with the deeper penetration for the higher collision energy. The smaller percentage of desorption for $\theta_I = 65°$, at each collision energy, is quite interesting.

Average final energies $\langle E_F \rangle$ of the trapped Xe atoms are listed in Table 2. The final energies are similar for θ_I of 0 and 25°, somewhat higher for θ_I of 45°, and decidedly higher for θ_I of 65°. On average the trapped Xe atoms lose 99.40, 99.03, 98.70, and 87.18% of their collision energy for $\theta_I = 0$, 25, 45, and 65°, respectively. Final energy distributions of the trapped Xe atoms are given in Figure 8 for θ_I of 0 and 25°. The average thermal energy of a trapped Xe-atom is $3k_B T_s/2$, where T_s is the surface temperature of 140 K. This energy is 18.1 meV and the numbers in Table 2 show that, for θ_I of 0 and 25°, the Xe atoms are close to being thermalized at the termination of the trajectories at 6 ps. The water molecules of the ice structure

Table 2. Average Final Translational Energies $\langle E_F \rangle$ of Trapped Xe Atoms^a

E_I(eV)/θ_I (degrees)	0	25	45	65
3.88	26.9 (23.5)^b	26.9	75.9	106
4.56	24.1 (21.4)	27.5	51.6	693
5.71	26.3 (22.0)	26.3	44.8	932
6.50	25.5 (24.0)	24.0	83.1	1106

^{a}The average Xe translational energy, $\langle E_F \rangle$, in meV at the termination of the trajectory at 6 ps. ^{b}The values of $\langle E_F \rangle$ for Xe/TIP3P ice collision are provided in parentheses.
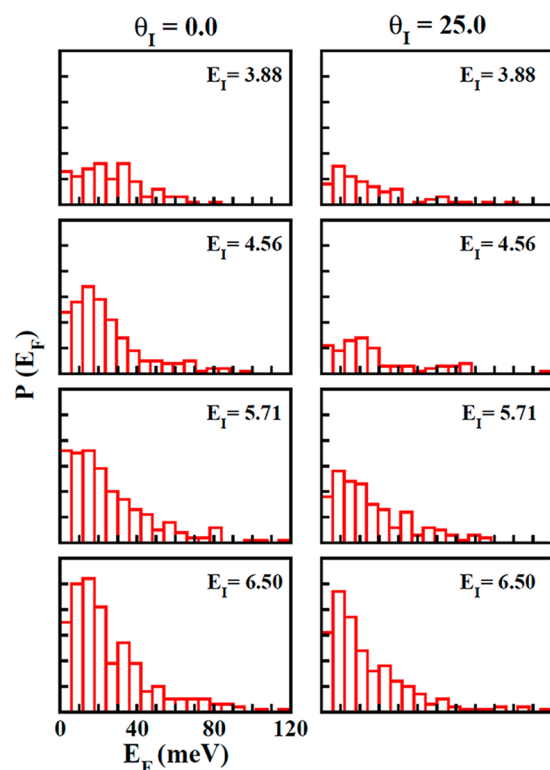

Figure 8. Translational energy distributions of the trapped Xe atoms at the end of 6 ps simulation trajectories. Results are reported for $\theta_I = 0$ and 25°, with varying E_I's. The scaling of the axes is same for all eight plots.

impacted by the Xe projectile absorb a large amount of the kinetic energy, and this energy is cascaded to adjacent water molecules. This phenomenon is quite different from simple binary collisions where the dynamics is in the keV energy regime. The penetration of Xe, an oversized projectile particle, into the crystalline ice surface is possible because the ice structure is soft and open, which permits water molecules to be pushed aside easily by the incoming projectile without effective collective recoil.[42]

A particularly interesting phenomenon is the less efficient equilibration of the Xe atoms impacting the surface with large incident angles and as a result a higher average translational energy for these trapped atoms at the 6 ps termination of the trajectories. This indicates that when the energy of the trapped Xe atom is in the x and y components, in contrast to the z component (Figure 1), energy relaxation is less efficient. Models[45,46] based on the residence time of the projectile with the surface are incomplete because this time is the same for the different θ_I. It is possible that the number of collisions between a trapped Xe atom and the water molecules[21,45] varies for the different θ_I. The role of θ_I, and its dynamics, for relaxation of the trapped Xe atoms is an interesting topic for future studies.

In a more detailed way, we have analyzed the depth of the trapped Xe atoms along the normal of the {0001} ice surface for the $\theta_I = 0°$ simulations. As shown in Table 3, the fractions of Xe atoms trapped within the bilayers are higher than in between two bilayers. There are increased van der Walls interactions between the Xe atoms and the water molecules within a bilayer, and the Xe atoms are apparently most energetically stable at these regions of the ice surface. This is in accord with observations by Mitlin et al.,[38] using potential of mean force calculations, where they identified adsorption sites for Xe atoms on water bilayers and the presence of high energy regions between these adsorption sites.

C. Scattering of Xe Atoms. Average values of the scattering angle $\langle \theta_F \rangle$ are listed in Table 4 for the different

Table 4. Average Velocity Scattering Angle $\langle \theta_F \rangle$ of Scattered Xe Atoms^a

E_I(eV)/θ_I (degrees)	0	25	45	65
3.88	28.5 (27.3)^c	28.2	32.3 [15.2%]^b	32.5 [70.4%]
4.56	30.5 (29.8)	27.5	33.3 [8.0%]	59.8 [74.1%]
5.71	31.1 (29.2)	29.6	32.5 [4.5%]	60.6 [71.1%]
6.50	30.4 (28.6)	29.7	33.6 [4.0%]	61.5 [65.2%]

^{a}The velocity scattering angle (in degrees) is the angle between the velocity vector of the scattered Xe atom and surface normal. Both directly scattered Xe atoms and those which penetrate the surface and desorb are included in analyses. The reported average velocity scattering angle is the average θ_F for the probability distribution of θ_F, i.e. $P(\theta_F)$. ^{b}The percentage of direct scattering trajectories, which was observed for θ_I =45, and 65°. ^{c}The values in parentheses are for the Xe/TIP3P ice collision dynamics.

E_I,θ_I combinations. Events in which the Xe atoms directly scatter off the surface without penetration and events with penetration followed by desorption are included in the analyses (the former events are discussed separately below). The fraction of the scattering that is direct (with respect to the total number of trajectories) is given in parentheses in Table 4. For isotropic scattering the θ_F distribution is proportional to

Table 3. Percentages of Trapped Xe Atoms Remaining at Different Depths^a

E_I (eV)	first BL	first-second BL	second BL	second-3rdBL	third BL
3.88	12.2 (37.6)^b	3.1(4.9)	13.5(24.1)	1.4 (1.9)	0.0(0.0)
4.56	13.5 (29.6)	1.83 (9.8)	30.8 (34.1)	1.6 (3.8)	0.0 (0.0)
5.71	9.6 (22.3)	5.4 (4.1)	38.6 (45.6)	7.2 (12.7)	0.0 (3.5)
6.50	8.2 (15.5)	3.7 (5.5)	38.5 (40.4)	8.4 (19.8)	14.2 (7.5)

^{a}The results are for the simulations with $\theta_I = 0°$ and recorded at the termination of the trajectories at 6 ps. 1st BL is the first bilayer and 1st−2nd BL is between the 1st and 2nd bilayers. ^{b}The results for Xe/TIP3P ice collision are in parentheses.

2188

dx.doi.org/10.1021/jp3112028 | *J. Phys. Chem. C* 2013, 117, 2183–2193

$\sin\theta\cos\theta$ and the average value is 45°. The values of $\langle\theta_F\rangle$ are significantly less than this value for $\theta_I = 0$, 25, and 45° showing that Xe atoms scatter preferentially in the direction of the surface normal. For the $\theta_I = 65°$ simulations and the three larger E_I, $\langle\theta_F\rangle$ is much larger than 45° and approximately the same as θ_I indicative of specular scattering. The scattering angle distributions are similar for θ_I of 0, 25, and 45°, and independent of E_I. Figure 9 gives the scattering angle distributions for θ_I of 0 and 65°. No scattering was observed beyond $\theta_F = 80.0°$ for any of the θ_I.
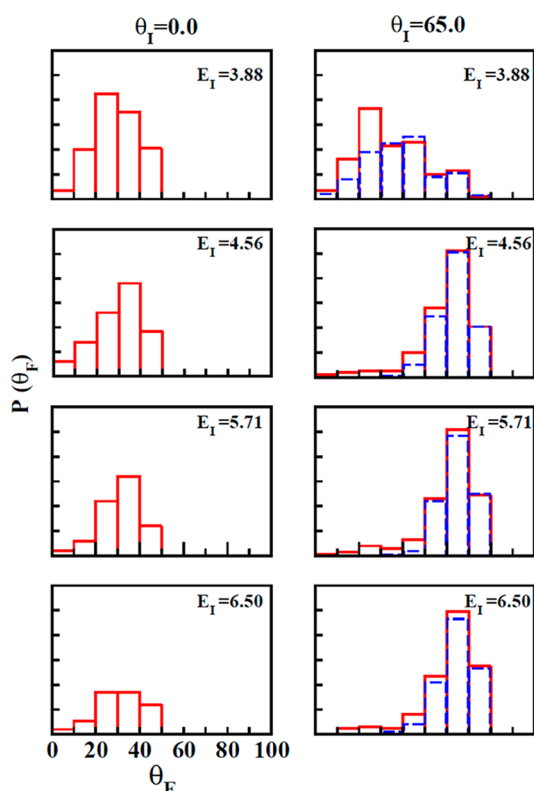

Figure 9. Probability of the velocity scattering angle versus θ_F, $P(\theta_F)$, which includes directly scattered Xe atoms and those that penetrate the ice and then desorb. Results are reported for $\theta_I = 0$ and 65°, with varying E_I's. The dashed lines give the velocity scattering angle probability for the directly scattered Xe-atoms without penetration. The scaling of the axes is same for all eight plots.

The average translational energy of the scattered Xe atoms $\langle E_F\rangle$ is plotted versus θ_F in Figure 10 for the different θ_I and their associated E_I. For θ_I of 0 and 25°, the value of $\langle E_F\rangle$ is highest when θ_F is very close to normal, that is <10°, and then gradually decreases for higher values of θ_F. The value of $\langle E_F\rangle$ is expected to be related to the depth of penetration of the incident Xe and the resulting number of collisions of the Xe atom with water molecules inside the ice. For θ_I of 0 and 25°, the simulation results indicate that the Xe atoms scattered at higher values of θ_F are colliding with multiple water molecules inside the ice surface, before desorbing, and therefore losing more energy compared to the Xe atoms which scatter at low θ_F. Another possible dynamical effect is a suggestion from the plots for $\theta_I = 0$ and 25° that the average value of $\langle E_F\rangle$ decreases with increase in E_I, which would be consistent with deeper penetration of the ice surface and more energy relaxation with increase in E_I. However, more analyses and better statistics are needed to confirm this. For θ_I of 45 and 65°, the value of

$\langle E_F\rangle$ increases with θ_F instead of decreasing as found for $\theta_I = 0$ and 25°. For θ_I of 45 and 65°, $\langle E_F\rangle$ is less than 250 meV for θ_F varying from 0 to 40 degrees, but after that $\langle E_F\rangle$ rapidly increases to values that are $\sim^1/_3$ to $^1/_2$ the collision energy. Between θ_I of 25 and 45° the form of the plot of $\langle E_F\rangle$ versus θ_F is expected to undergo a transition of what is found here for $\theta_I = 0$ and 25° and $\theta_I = 45$ and 65°.

Models have been presented for representing $\langle E_F\rangle$ versus E_I with all the θ_F included.[46,47] It would be on interest to consider these models for the Xe + ice collisions, but results for more E_I are needed. This is a possible investigation for future studies.

As shown in Figure 6, for $\theta_I = 0$ and 25° each of the colliding Xe atoms penetrates the ice surface and there is no direct scattering. Thus, for these incident angles all of the scattering involves penetration followed by desorption. However, for $\theta_I = 45$ and 65° direct scattering becomes important and these dynamics are discussed in the next section.

D. Scattering without penetration. For $\theta_I = 45$ and 65° a significant number of the Xe-atoms directly scatter without penetrating the ice surface. For $\theta_I = 45°$ the percentage of the total number of trajectories that undergo direct scattering without penetration is 15, 8.0, 4.5, and 4.0% for $E_I = 3.88$, 4.56, 5.71, and 6.50 eV, respectively. However, for the more grazing incident angle of $\theta_I = 65°$ these respective percentages are much higher and 70, 74, 71, and 65%. Direct scattering favors approximate specular scattering, with θ_F the same as θ_I. This is illustrated in Figure 9 for the simulations at $\theta_I = 65°$.

On average, the directly scattered trajectories retain more energy in Xe translation than do those which penetrate and desorb. For $\theta_I = 45°$ the penetrate-desorb/direct $\langle E_F\rangle$ values are 95/336.5, 130.3/447.2, 110.7/625.4 for $E_I = 3.88$, 4.56, 5.71, and 6.50 eV, respectively. For $\theta_I = 65°$, these respective values are 110.4/1071.9, 128/1180.6, 125/1412, and 553.3/1673.8. The $\langle E_F\rangle$ values are much larger for the directly scattered Xe-atoms. The value of $\langle E_F\rangle$ for thermal desorption, that is $2k_BT_s$, is quite small and 24 meV.

In simulations of collisions of rare gas atoms and diatomic and triatomic molecules with SAM surfaces, it is found that thermal accommodation with the surface may be achieved by directly scattered atoms/molecules.[45,46,48−50,53] Such dynamics is not found here for the directly scattered Xe-atoms, which may result from the high collision energies and the short interaction/residence times of the atoms with the ice surface.

E. Desorption Kinetics. As discussed above in section III.B, for each θ_I, E_I an appreciable fraction of the Xe atoms, which penetrate the ice surface, desorb during the 6 ps trajectory integrations. Of interest is whether this desorption occurred early or late during the trajectory integration, and if there is a relationship between the time of the desorption and the translational energy E_F of the desorbed Xe atom. In Figure 11, the probabilities that the desorption occurred in either the 0−1, 1−2, 2−3, 3−4, 4−5, or 5−6 ps time interval are plotted for the different θ_I and $E_I = 6.50$ eV (the time the Xe atom hits the top of the ice surface is around 0.24 ps for $E_I = 6.50$ eV). For each θ_I, there is a well-defined peak in the probability distribution, with the height of the peak varying from ~40−65%. In comparing the probabilities for the different θ_I, it is seen that the peak in the probability distribution smoothly moves from 0 to 1 ps for $\theta_I = 65°$ to 2−3 ps for $\theta_I = 0°$. For $\theta_I = 0$ and 25°, there are no desorptions in the 0−1 ps time interval, and for $\theta_I = 65°$ there are no desorptions in the 5−6 ps time interval. An important feature of the probability distributions is the small amount of desorption for the longer integration times of 4−6
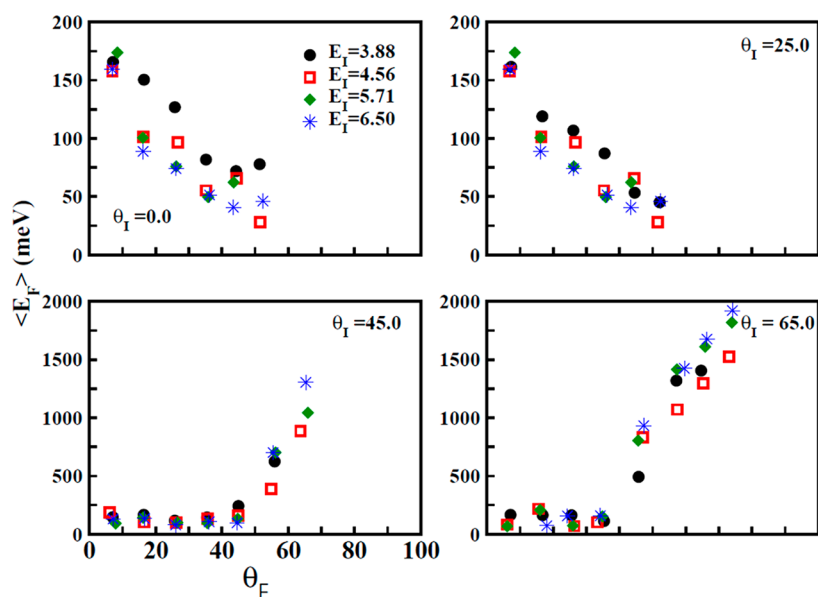
Figure 10. Average translational energies $\langle E_F \rangle$ of the scattered Xe-atoms versus the scattering angle θ_F. Results are reported for different combinations of E_I, θ_I. Scaling of the x axis is the same for all four plots.
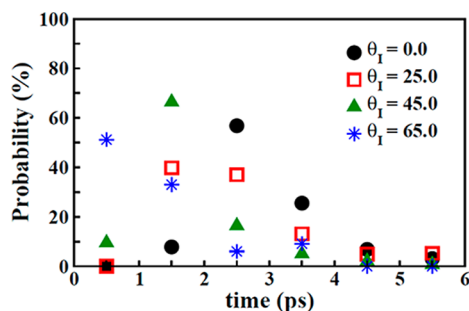

Figure 11. Probabilities that desorption occurred in either the 0−1, 1−2, 2−3, 3−4, 4−5, or 5−6 ps time interval for the different θ_I and E_I = 6.50 eV. For θ_I = 0 and 25° there is no desorption in the 0−1 ps time interval, and for θ_I = 65° there is no desorption in the 5−6 ps time interval.
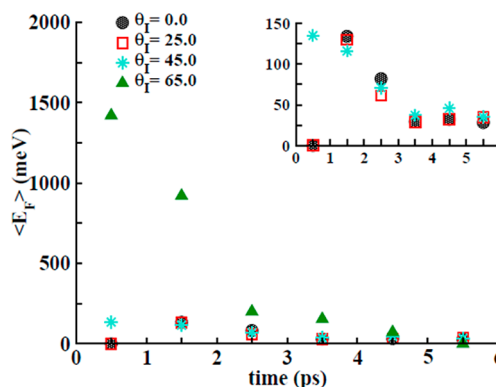

Figure 12. Plots of the average translational energy $\langle E_F \rangle$ of the desorbing Xe atoms versus the desorption time for the simulations in Figure 11. The insert in this figure clearly shows $\langle E_F \rangle$ vs desorption time (ps) for θ_I = 0, 25, and 45°.

ps with θ_I = 0, 25, and 45° suggesting that desorption becomes less important for longer times.

In Figure 12 the average translational energy $\langle E_F \rangle$ of the desorbing Xe atoms is plotted versus the desorption time for the simulations in Figure 11. The former figure shows there is a relationship between the peak in the probability distribution in Figure 11 and the translational energies E_F of the desorbing Xe atoms. For longer times where the desorption probability is low, $\langle E_F \rangle$ is small. To illustrate, for θ_I = 0° the $\langle E_F \rangle$ values are 134, 82, 29, 32, and 28 meV for the 1−2, 2−3, 3−4, 4−5, and 5−6 ps time intervals, respectively. In comparison the $2k_B T_s$ value for thermal desorption is 24 meV. The relationship between the thermalization of a colliding projectile and its residence/interaction time with the surface has been discussed previously[45,46] and the results in Figure 12 are consistent with this earlier work. For long residence times there may be a close relationship with the number of collisions the projectile has with the surface.[21,45]

F. TIP3P Simulation Results. Simulations were performed using the TIP3P potential for the ice surface to compare with the above results for the TIP4P potential. The TIP3P simulations are done for θ_I = 0° and E_I = 3.88, 4.56, 5.71,

and 6.50 eV, values also studied with TIP4P. With TIP3P all of the colliding Xe atoms penetrate the ice surface, the same result found with TIP4P. The fractional depths of penetration in terms of the first, first-2nd, second, second-3rd, third, third-4th bilayer regions are 0.10, 0.25, 0.61, 0.04, 0.00, 0.00 for E_I = 3.88 eV; 0.02, 0.11, 0.77, 0.10, 0.00, 0.00 for E_I = 4.56 eV; 0.00, 0.02, 0.55, 0.42, 0.01, 0.00 for E_I = 5.71 eV; and 0.00, 0.00, 0.39, 0.40, 0.20, 0.01 for E_I = 6.50 eV. These results are very similar to those found for TIP4P, as shown in Figure 6. Penetration becomes deeper with increasing E_I for the TIP3P model.

The percentage of the Xe-atoms that remain trapped at the termination of the trajectory integration at 6 ps is larger with TIP3P as shown in Figure 7. At E_I = 3.88 eV, trapping with TIP3P is 2.3 times larger than with TIP4P and at E_I = 6.50 eV this ratio is 1.2. The bilayer regions at which the trajectories are trapped at 6 ps are identified in Table 3, where they are compared with the TIP4P results. The average translational energies of the trapped Xe-atoms are listed in Table 2. They are similar too, but slightly smaller than the TIP4P values. Apparently the TIP3P potential enhances relaxation of the Xe-atoms as compared to the TIP4P potential. The TIP3P

average velocity scattering angles are compared with the TIP4P values in Table 4. They are similar, but the TIP3P scattering is slightly closer to the surface normal.

IV. COMPARISON WITH EXPERIMENT

Previously,[23] experimental and simulation values of $\langle E_F \rangle$ versus θ_F were compared for $E_I = 6.50$ eV and $\theta_I = 0$ and 65°. Quite good agreement is found between experiment and simulation for $\theta_I = 65°$, where direct scattering predominates. The experimental and simulation plots of $\langle E_F \rangle$ versus θ_F are compared in Figure 13 for $E_I = 6.50$ eV and $\theta_I = 0°$, 25°, and
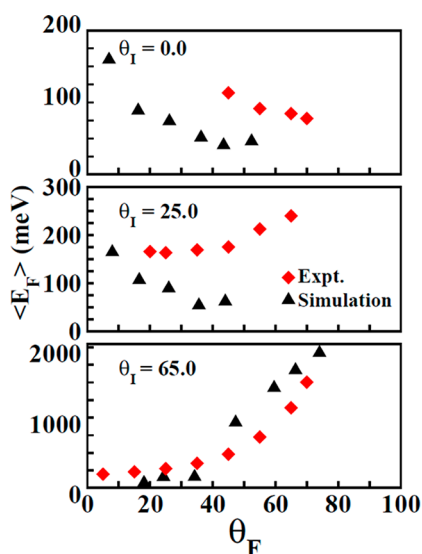

Figure 13. Comparison of the average value of the translational energy of the scattered Xe atoms, $\langle E_F \rangle$, versus the scattering angle θ_F, derived from simulation and experiment. Results are given for $\theta_I = 0°$, 25°, and 65° and $E_I = 6.5$ eV (except for $\theta_I = 25°$ where the experimental E_I is 6.4 eV). The experimental results are for crystalline ice.

65°. For $\theta_I = 0°$ there is quite good agreement between simulation and experiment as found for $\theta_I = 65°$. At $\theta_I = 25°$, experiment and simulation agree only for θ_F near 0°, and for larger θ_F they disagree. The $\langle E_F \rangle$ values from the simulations sharply decrease with increase in θ_F and in contrast they slightly increase in the experiments. A striking feature of the $\langle E_F \rangle$ versus θ_F plots is the difference between the shapes of the plots for $\theta_I = 0$ and 65°. The simulation plot for $\theta_I = 25°$ is of the same form as that for $\theta_I = 0°$, and the plot for $\theta_I = 45°$ (Figure 10) is of the same form as that for $\theta_I = 65°$. Thus, for some simulation angle(s) between $\theta_I = 25°$ and 45° there will be a transition between the two forms of the $\langle E_F \rangle$ versus θ_F plot and it may be very similar to the experimental plot at $\theta_I = 25°$. As a result, the transition between the two forms of the $\langle E_F \rangle$ versus θ_F plot in the simulations will occur at a larger θ_I than in the experiments. In our previous work, it was suggested that such a difference may be due to differences between the surfaces in the simulations and experiments,[23] with the experiments consistent with a much more disordered ice structure as compared to the ordered structure for the simulations. This suggestion is consistent with other studies.[51]

The greater disorder of the experimental ice structure as compared to that for the simulations is expected to increase the amount of direct scattering in the experiments relative to the simulations. This may explain two differences between the experimental and simulation scattering discussed above. The

larger experimental $\langle E_F \rangle$ values versus θ_F for $\theta_I = 0°$, as compared to the simulations, is consistent with some direct scattering in the experiments (none is observed in the simulations). The transition between the two forms of the $\langle E_F \rangle$ versus θ_F plot, with increase in θ_I, is expected to arise from an increase in direct scattering. With this increase more pronounced for the experiments, this transition is expected to occur at a smaller θ_I for the experiments, the result found here.

The experimental translational energy distribution of the scattered Xe atoms, $P(E_F)$, may be fit by a two-component model[22] with a slow component given by the Maxwell–Boltzmann distribution for thermal desorption at the surface temperature $T_s = 140$ K and a fast component given by a shifted Maxwell–Boltzmann distribution with a fitted temperature.[52,53,54] The largest number of scattering events were observed for $E_I = 3.88$ eV and $\theta_I = 25°$ and a test was made to determine if $P(E_F)$ of the scattered Xe atoms could be fit with the two-component function. The result is shown in Figure 14,
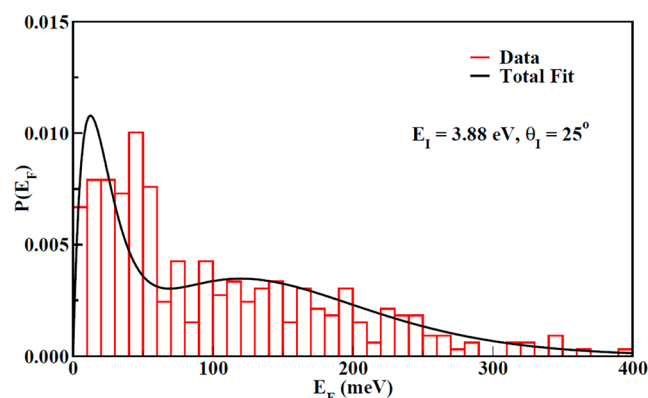

Figure 14. Final energy distribution (histogram) of all scattered Xe atoms at $E_I = 3.88$ eV and $\theta_I = 25°$. A bimodal fitting, consisting of Maxwell–Boltzmann and shifted Maxwell–Boltzmann velocity distribution functions, is illustrated.

which illustrates that the simulation $P(E_F)$ of all the scattered Xe atoms may be approximately fit by the same two-component function as used for the experiments. The probability for the slow component is 39%, and the velocity shift and temperature for the fast component are 328.5 m/s and $T = 329$ K, respectively. To obtain a quantitative $P(E_F)$ and make a direct comparison with experiment, many more trajectories are required.

The simulation trapping probabilities are found to be higher than the experimental results, which may be attributed in part to the higher degree of energy transfer to the ice surface in the simulations. A similar observation was reported by Anderson et al.[19]

IV. CONCLUSIONS

In this article, simulation results are presented for Xe atoms colliding with the {0001} I_h ice surface with energies E_I of 3.88, 4.56, 5.71, and 6.50 eV and incident angles θ_I of 0, 25, 45, and 65°. The goal of the simulations is to obtain an atomistic understanding of the energy transfer, penetration, and trapping dynamics of the Xe atoms, and to compare with experimental studies.[23] The following general findings are obtained using the TIP4P model for the potential energy of the ice surface:

(1) Three types of events are observed in the Xe−ice surface collisions; that is penetration into the surface and then

desorption, penetration into the surface with Xe remaining trapped in the surface at the conclusion of the 6 ps trajectory, and direct scattering off without surface penetration.

(2) Surface penetration is most probable for normal $\theta_I = 0°$ collisions and direct scattering without penetration becomes important for $\theta_I = 45$ and $65°$. Penetration into the ice surface becomes deeper with increase in E_I. For $\theta_I = 0$ and $25°$ all the Xe atoms penetrate the surface and there is no direct scattering.

(3) The probability the colliding Xe atoms remain trapped in the surface, at the conclusion of the 6 ps trajectory, increases with E_I, and is more than 70% for $\theta_I = 0°$ and $E_I = 6.50$ eV. The water molecules of the ice structure impacted by the Xe projectile absorb a large amount of the kinetic energy, and this energy is rapidly dissipated to adjacent water molecules through the hydrogen bonding network. The average thermal energy of a trapped Xe-atom is $3k_B T_s/2 = 18.1$ meV, where T_s is the surface temperature of 140 K. For θ_I of 0 and $25°$, the trapped Xe atoms have an energy of 24−27 meV at 6 ps, for the E_I, and are close to being thermalized at the termination of the trajectories. Trapping is more favorable at an ice bilayer than between bilayers, which is consistent with a previous study.[38]

(4) For $\theta_I = 0, 25$, and $45°$ the average values of the velocity scattering angle $\langle\theta_F\rangle$ are significantly less than the value of $45°$ for isotropic scattering, showing the Xe atoms scatter preferentially in the direction of the surface normal. For the $\theta_I = 65°$ simulations, $\langle\theta_F\rangle \sim \theta_I$ indicative of specular scattering.

(5) For θ_I of 0 and $25°$ the average translational energy of the scattered Xe-atoms $\langle E_F\rangle$ versus θ_F is highest when θ_F is very close to normal, that is $<10°$, and then gradually decreases for higher values of θ_F. For these θ_I there is an indication that $\langle E_F\rangle$ decreases with increase in E_I, which is consistent with deeper penetration of the ice surface and more energy relaxation with an increase in E_I. For θ_I of 45 and $65°$, $\langle E_F\rangle$ is less than 250 meV for θ_F varying from 0 to 40 degrees, but for larger θ_F the value of $\langle E_F\rangle$ rapidly increases to $\sim^1/_3$ to $^1/_2$ the collision energy. Between θ_I of 25 and $45°$ the form of the plot of $\langle E_F\rangle$ versus θ_F is expected to undergo a transition of what is found here for $\theta_I = 0$ and $25°$ and $\theta_I = 45$ and $65°$.

(6) There is a well-defined peak, within the 0−3 ps time interval, of the desorption probability versus time for the penetrating Xe atoms. The area of this peak is as large as $\sim$65% for a 1 ps time interval, showing that most of the desorption occurs within a narrow time window. An important feature of these probability distributions is the small amount of desorption for the times of 4−6 ps suggesting that desorption becomes less important for longer times. The decreased desorption at longer times is consistent with the enhanced thermalization of the trapped Xe atoms at longer times.

(7) An interesting finding is that themalization of the trapped Xe atoms depends on θ_I. As discussed above for θ_I of 0 and $25°$ the average energy of the trapped Xe atoms at the 6 ps conclusion of the trajectories is 24−27 meV, independent of E_I, and close to the surface thermal kinetic energy of 18.1 meV. In contrast, the average energy of the trapped Xe atoms at 6 ps is much higher for θ_I of 45 and $65°$; $\sim$40−80 meV for $\theta_I = 45°$ and as

high as $\sim$1100 meV for $\theta_I = 65°$ and $E_I = 6.50$ eV. Complete thermalization of the trapped Xe atoms takes more than 6 ps and has a strong dependence on θ_I, an intriguing topic to investigate in future studies.

(8) Simulation results using the TIP3P model for the ice surface are similar to those above for the TIP4P model, with the caveat that trapping in the ice surface is more pronounced for the TIP3P model.

(9) As described above, the simulation results are in overall quite good agreement with experiment.

■ AUTHOR INFORMATION

Corresponding Author
*E-mail: bill.hase@ttu.edu.

Present Address
†Chemistry Department, Loyola University Chicago, Illinois 60626, United States.

Notes
The authors declare no competing financial interest.

■ REFERENCES

(1) Lowe, D.; MacKenzie, A. R. *J. Atmos. Sol.-Terr. Phys.* **2008**, *70*, 13−40.
(2) Fan, S. M; Jacob, D. J. *Nature* **1992**, *359*, 522−524.
(3) Greenberg, J. M. *Surf. Sci.* **2002**, *500*, 793−822.
(4) Horn, A. B.; Chesters, M. A.; McCoustra, M. R. S.; Sodeau, J. R. *J. Chem. Soc., Faraday Trans.* **1992**, *88*, 1077−1079.
(5) Eichler, B.; Zimmerman, H. P.; Gaggeler, H. W. *J. Phys. Chem. A* **2000**, *104*, 3126−3131.
(6) Schaff, J. E.; Roberts, J. T. *Langmuir* **1998**, *14*, 1478−1486.
(7) Sadtchenko, V.; Knutsen, K.; Giese, C. F.; Gentry, W. R. *J. Phys. Chem. B* **2000**, *104*, 2511−2521.
(8) Dohnalek, Z.; Ciolli, R. L.; Kimmel, G. A.; Stevenson, K. P.; Smith, R. S.; Kay, B. D. *J. Chem. Phys.* **1999**, *110*, 5489−5492.
(9) Glebov, A.; Graham, A. P.; Menzel, A.; Toennies, J. P. *J. Chem. Phys.* **1997**, *106*, 9382−9385.
(10) Braun, J.; Glebov, A.; Graham, A. P.; Menzel, A.; Toennies, J. P. *Phys. Rev. Lett.* **1998**, *80*, 2638−2641.
(11) Gotthold, M. P.; Sitz, G. O. *J. Phys. Chem B* **1998**, *102*, 9557−9564.
(12) Brown, D. E; George, S. M.; Huang, C.; Wong, E. K. L.; Rider, K. B.; Smith, R. S.; Kay, B. D. *J. Phys. Chem.* **1996**, *100*, 4988−4995.
(13) Isaksson, M. J.; Sitz, G. O. *J. Phys. Chem. A* **1999**, *103*, 2044−2049.
(14) Rieley, H.; Aslin, H. D.; Haq, S. *J. Chem. Soc. Faraday Trans.* **1995**, *91*, 2349−2351.
(15) Inamura, M.; Takaoka, T.; Komeda, T. *Surf. Sci.* **2007**, *601*, 1072−1078.

(16) Gibson, K. D; Killelea, D. R.; Yuan, H.; Becker, J. S.; Sibener, S. J. *J. Chem. Phys.* **2011**, *134*, 034703-1- 034703-7.

(17) Pietrass, T.; Gaede, H. C.; Bifone, A.; Pines, A.; Ripmeester, J. A. *J. Am. Chem. Soc.* **1995**, *117*, 7520−7525.

(18) Moudrakovski, I. L.; Sanchez, A. A.; Ratcliffe, C. I.; Ripmeester, J. A. *J. Phys. Chem. B* **2001**, *105*, 12338−12347.

(19) Gibson, K. D; Killelea, D. R; Becker, J. S.; Yuan, H.; Sibener, S. J. *Chem. Phys. Lett.* **2012**, *531*, 18−21.

(20) Anderson, P. U.; Nagard, M. B.; Bolton, K.; Svanberg, M.; Pettersson, J. B. C. *J. Phys. Chem. A* **2000**, *104*, 2681−2688.

(21) Tasić, U. S.; Yan, T. Y.; Hase, W. L. *J. Phys. Chem. B* **2006**, *110*, 11863−11877.

(22) Tasić, U.; Troya, D. *Phys. Chem. Chem. Phys.* **2008**, *10*, 5776−5786.

(23) Gibson, K. D; Killelea, D. R.; Yuan, H.; Becker, J. S.; Pratihar, S.; Paranjothy, M.; Kohale, S. C.; Hase, W. L.; Sibener, S. J. *J. Phys Chem. C* **2011**, *116*, 14264−14273.

(24) Neil Gardner, D. O.; Al-Halabi, A.; Kroes, G.-J. *J. Chem. Phys.* **2004**, *120*, 11796−11803.

(25) Al-Halabi, A.; Kleyn, A. W.; Kroes, G.-J. *J. Chem. Phys.* **2001**, *115*, 482−491.

(26) Jorgensen, W. L.; Chandrashekhar, J.; Madura, J. D.; Impey, R. W.; Klein, M. L. *J. Chem. Phys.* **1983**, *29*, 926−935.

(27) Jorgensen, W. L.; Madura, J. D. *Mol. Phys.* **1985**, *56*, 1381−1392.

(28) Tanaka, H. *J. Chem. Phys.* **1998**, *108*, 4887−4893.

(29) Wilson, M. A.; Pohorille, A.; Jenniskens, P.; Blake, D. F. *Origins Life Evol. Biosphere* **1995**, *25*, 3−19.

(30) Kroes, G.-J. *Surf. Sci.* **1992**, *275*, 365−382.

(31) Clary, D. C.; Wang, L. *J. Chem. Soc., Faraday Trans.* **1997**, *93*, 2763−2767.

(32) Kroes, G.-J.; Clary, D. C. *J. Phys. Chem.* **1992**, *96*, 7079−7088.

(33) Shivaglal, M. C; Brakaspathy, R.; Singh, S. *Proc. Ind. Acad. Sci.* **1988**, *100*, 413−424.

(34) Hayward, J. A.; Reimers, J. R. *J. Chem. Phys.* **1997**, *106*, 1518−1529.

(35) Lahaye, R. J. W. E. *Surf. Sci.* **2010**, *604*, 1135−1142.

(36) Hay, P. J.; Wadt, W. R. *J. Chem. Phys.* **1985**, *82*, 270−283. Hay, P. J.; Wadt, W. R. *J. Chem. Phys.* **1985**, *82*, 284−298. Hay, P. J.; Wadt, W. R. *J. Chem. Phys.* **1985**, *82*, 299−310.

(37) Simon, S.; Duran, M.; Dannenberg, J. J. *J. Chem. Phys.* **1996**, *105*, 11024−11031.

(38) Miltin, S.; Lemak, A. S; Torrie, B. H.; Leung, K. T. *J. Phys. Chem. B* **2003**, *107*, 9958−9963.

(39) Hase, W. L.; Duchovic, R. J.; Hu, X.; Kormonicki, A.; Lim, K.; Lu, D.-H.; Peslherbe, G. H.; Swamy, N. K.; Vande Linde, S. R.; Varandos, A. J. C.; Wang, H.; Wolfe, R. J. *QCPE Bull.* **1996**, *16*, 671.

(40) X. Hu, X.; Hase, W. L.; Pirraglia, T. *J. Comput. Chem.* **1991**, *12*, 1014−1024.

(41) Bosio, S. B. M.; Hase, W. L. *J. Chem. Phys.* **1997**, *197*, 9677−9686.

(42) Bosio, S. B. M.; Hase, W. L. *Int. J. Mass Spectrom. Ion Process.* **1998**, *174*, 1−9.

(43) Allen, M. P.; Tildesley, D. J. *Computer Simulation of Liquids*; Oxford University Press: New York, 1989.

(44) Bolton, K.; Svanberg, M.; Pettersson, J. B. C. *J. Chem. Phys.* **1999**, *110*, 5380−5391.

(45) Yan, T.; Hase, W. L. *Phys. Chem. Chem. Phys.* **2000**, *2*, 901−910.

(46) M-Palacios, M.; Nogueira, J. J; M-Nunez, E. *J. Phys. Chem. C* **2012**, *116*, 25454−25464.

(47) Yang, L.; Mazyar, O. A.; Lourderaj, U.; Wang, J.; Rodgers, M. T.; M-Nunez, E.; Addepalli, S. V.; Hase, W. L. *J. Phys. Chem. C* **2008**, *112*, 9377−9386.

(48) Yan, T.; Isa, N.; Gibson, K. D; Sibener, S. J.; Hase, W. L. *J. Phys. Chem. A* **2003**, *107*, 10600−10607.

(49) Isa, N.; Gibson, K. D.; Yan, T.; Hase, W.; Sibener, S. J. *J. Chem. Phys.* **2004**, *120*, 2417−2433.

(50) M-Nunez, E.; Rahman, A.; Hase, W. L. *J. Phys. Chem. C* **2007**, *111*, 354−364.

(51) Yan, T.; Hase, W. L.; Tully, J. C. *J. Chem. Phys.* **2004**, *120*, 1031−1043.

(52) Tasić, U. S.; Day, B. S.; Yan, T. Y.; Morris, J. R.; Hase, W. L. *J. Phys. Chem. C* **2008**, *112*, 476−490.

(53) Peng, Y.; Liu, L.; Cao, Z.; Li, S.; Mazyar, O. A.; Hase, W. L.; Yan, T. *J. Phys. Chem. C* **2008**, *112*, 20340−20346.